Energy Storage Materials 89 (2026) 105231

Contents lists available at ScienceDirect

Energy Storage Materials

journal homepage: www.elsevier.com/locate/ensm

Chemomechanical Stability Determines the Performance of Dry-Processed Cathode and Separator Sheets in Thiophosphate-Based Solid-State Batteries

Maik Schmitt [a], Pascal Dippell [b], Philip Henkel [a], Ruizhuo Zhang [a], Peer Räke [a], Jürgen Janek [a,b], Marcus Rohnke [b], Aleksandr Kondrakov [a,c], Torsten Brezesinski [a,*], Florian Strauss [a,*]

[a] Battery and Electrochemistry Laboratory (BELLA), Institute of Nanotechnology, Karlsruhe Institute of Technology (KIT), Kaiserstr. 12, 76131 Karlsruhe, Germany
[b] Institute of Physical Chemistry & Center for Materials Research, Justus Liebig University Giessen, Heinrich-Buff-Ring 17, 35392 Giessen, Germany
[c] BASF SE, Carl-Bosch-Str. 38, 67056 Ludwigshafen, Germany

ARTICLE INFO

Keywords:
Energy storage
Solid-state batteries
Dry-processing

ABSTRACT

Dry processing has recently emerged as a promising solvent-free manufacturing strategy for solid-state batteries (SSBs). In this work, we systematically investigate how dry-processed $LiNi_{0.85}Co_{0.1}Mn_{0.05}O_2$ cathode and Li_6PS_5Cl solid electrolyte (SE) separator sheets influence performance and degradation in different SSB architectures. They were produced using a fibrillating polytetrafluoroethylene (PTFE) binder and compared to conventional powder-based (pelletized) configurations. In addition, various cathode formulations were investigated to elucidate the effect that both carbon black and protective surface coating of the cathode active material (CAM) have on cycling performance. It is demonstrated that introducing a fibrillar network improves particle-particle contact and mechanical integrity, resulting in higher initial capacities, better rate capability, and increased Coulomb efficiency compared to pelletized cells. However, the experimental data indicate that while carbon black improves electronic percolation, it simultaneously accelerates interfacial degradation in PTFE-containing SSB architectures. *Post mortem* characterization and *in situ* gas analysis further show that the sheet-type cathodes are subject to greater electrochemical degradation, but still perform better than their pelletized counterparts. Therefore, long-term cycling performance is determined more by chemomechanical stability than by the extent of SE degradation at the CAM|SE interface alone. Overall, this study provides mechanistic insights into the role of dry processing in thiophosphate-based cells, highlights both the advantages and limitations of PTFE as a binder, and offers design guidelines for future SSB manufacturing.

1. Introduction

Solid-state batteries (SSBs) are widely regarded as a promising technology for next-generation energy storage [1–3]. Compared to conventional lithium-ion batteries (LIBs) using liquid organic electrolytes, SSBs offer the potential for higher energy and power densities, improved thermal stability, and increased safety [2,4]. However, a major challenge for their large-scale commercialization remains the development of scalable manufacturing processes, as well as optimized electrode and separator architectures that maintain both mechanical and electrochemical integrity over extended cycling. Current processing strategies for SSB components are primarily based on either powder compression (cold pressing)[5] or slurry processing [6,7]. Both approaches offer distinct advantages, but also suffer from significant limitations.

Powder compression represents a simple, solvent-free technique that is widely used for laboratory-scale preparation of solid electrolyte (SE) and composite electrode layers [8]. In this approach, the SE separator and the cathode, typically consisting of the cathode active material (CAM), SE, and conductive additive(s), are uniaxially pressed under high mechanical pressure, often reaching several hundred MPa [9–12]. The applied pressure compacts the particles into dense pellets, thereby improving particle-particle contact and bulk ionic conductivity without the need for solvents, binders, or energy-intensive drying steps. However, this method exhibits several intrinsic drawbacks. The resulting pellets are mechanically fragile and prone to cracking, rendering them incompatible with continuous roll-to-roll manufacturing processes [8]. Furthermore, the high pressure required for densification can induce particle fracture, local stress accumulation, and interfacial damage, leading to microstructural defects that evolve into cracks and

* Corresponding authors.
E-mail addresses: torsten.brezesinski@kit.edu (T. Brezesinski), florian.strauss@kit.edu (F. Strauss).

https://doi.org/10.1016/j.ensm.2026.105231
Received 26 March 2026; Received in revised form 6 May 2026; Accepted 16 May 2026
Available online 17 May 2026

delamination during cycling [13,14]. In addition, only relatively thick electrode and separator layers (several hundred microns) can be produced, which limits the achievable energy density in practical applications [15–17]. Consequently, powder compression is primarily suited for fundamental studies rather than large-scale (industrial) fabrication.

In contrast, slurry processing, adapted from conventional LIB manufacturing, enables the preparation of composite electrode and separator sheets with controlled composition and uniform microstructure [18,19]. In this approach, the active material, SE, and conductive additive(s) are dispersed in a solution (e.g., toluene, ethanol, or N-methyl-2-pyrrolidone) containing the polymer binder to form a slurry [20,21]. This slurry is then cast onto a substrate or current collector, followed by solvent evaporation (vacuum drying) and calendaring to obtain dense electrode sheets [22]. This method ensures even particle distribution, tailorable film thickness, and strong mechanical cohesion, and it is compatible with industrial roll-to-roll processes [18,23]. However, the use of wet processing in combination with sulfide SEs is severely limited by their chemical instability in polar and protic solvents. Even exposure to nominally non-reactive, non-polar, and non-protic solvents can trigger side reactions in the presence of trace moisture and other impurities, eventually resulting in hydrolysis and oxidation of the SE and formation of undesired decomposition products, such as Li_2S, Li_2O, and H_2S [24–27]. In addition, the drying step during solvent removal can introduce microstructural inhomogeneities, such as porosity/voids or binder segregation, thus negatively affecting mechanical integrity and cycling performance [28–31]. Residual solvent may further promote interfacial degradation. Although wet processing enables straightforward integration of SSB manufacturing into existing LIB production lines, the reliance on organic solvents, energy-intensive drying procedures, and the high sensitivity of sulfide SEs somewhat hinder widespread application.

To overcome these challenges, dry processing has recently emerged as a promising alternative that combines the advantages of both approaches. This solvent-free method produces cohesive, yet flexible electrode and separator sheets without the use of volatile or toxic solvents, representing a sustainable and scalable manufacturing strategy. It offers the chemical compatibility of powder compression while providing the mechanical flexibility and scalability of film-based electrode preparation [32]. In this approach, a small amount of a fibrillating polymer binder, typically polytetrafluoroethylene (PTFE), is mechanically blended with the active material, SE, and conductive additive(s). Under shear stress, PTFE fibrillates and forms a continuous network that connects the particles, ensuring mechanical cohesion and structural integrity without the need for high compaction pressures or solvent evaporation [33–36]. The resulting composite films can be laminated or stacked under moderate pressure, eventually enabling thin, flexible, and roll-to-roll-compatible electrode architectures [37]. Aside from the mentioned processing advantages, it also affects the chemomechanical stability of SSB electrodes. The fibrillated binder network maintains intimate particle contact, effectively distributes stress during cycling, and mitigates crack propagation and interfacial delamination [36, 38–40]. Furthermore, the absence of solvents prevents undesired side reactions and preserves the chemical integrity of moisture- and oxygen-sensitive SEs, resulting in more stable interfaces and improved performance [4,41,42]. Overall, dry processing represents a next-generation manufacturing strategy that is capable of bridging the gap between laboratory-scale feasibility and industrial scalability, offering a sustainable pathway toward advanced SSBs [43]. For a comprehensive overview of dry-processing strategies and PTFE fibrillation, the reader is referred to the recent review by Han *et al.*[44]

In this work, we investigated the potential of dry processing for producing sheet-type SSBs. To elucidate the influence of electrode and separator architecture on cycling performance, various cell configurations were systematically compared. Furthermore, the impact of a surface coating and the role of a conductive additive were examined in the context of dry processing. Taken together, our study demonstrates how certain modifications at the material and processing level affect the stability of thiophosphate-based SSBs and further identifies key factors that make dry processing a promising manufacturing method.

2. Results and Discussion

In the present work, a solvent-free process based on the method described by Hippauf *et al.*[45] was used to produce the cathode and separator sheets. Fig. 1**a** illustrates the aforementioned procedure for the composite cathode on a laboratory scale. Initially, a powder mixture consisting of CAM ($LiNi_{0.85}Co_{0.1}Mn_{0.05}O_2$, NCM85), SE ($Li_6PS_5Cl$, LPSCl), and optional carbon black (Super C65) as a conductive additive was homogenized via mechanical milling and then combined with the desired amount of PTFE. Fibrillation of PTFE and formation of the cathode composite "dough" was achieved through sheer forces introduced during continuous grinding at 80°C for ~20 min using a mortar and pestle. Subsequently, the "dough" was rolled out to the desired thickness, followed by densification via calendaring. A representative photograph and a scanning electron microscopy (SEM) image of a cathode sheet are presented in Fig. 1**a**. In the SEM image, fibrillated PTFE can be readily identified, wrapping around the SE and CAM particles and connecting them to form the rubber-like mass.

The same process was used for the preparation of separator sheets. However, in that case, LPSCl was blended directly with the PTFE. First, different quantities of binder were tested to determine the optimum weight percentage that allows for easy processing and handling of the sheets while minimizing the reduction in ionic conductivity caused by the presence of PTFE. Specifically, binder fractions ranging from 0.2 to 1.0 wt.% were examined. The room-temperature ionic conductivity was determined by electrochemical impedance spectroscopy (EIS). The results are shown in Fig. 1**b**, together with the data for the binder-free separator for comparison. As expected, the ionic conductivity decreased with increasing PTFE fraction, from 2.35 mS cm^{-1} for the reference to 1.82 mS cm^{-1} for sheets containing 1 wt.% PTFE. This drop in ionic conductivity is due to the insulating properties of PTFE, which deteriorate ionic percolation within the SE separator. The optimal balance between mechanical integrity and ionic conductivity in the dry-processed sheets was achieved with 0.5 wt.% PTFE, maintaining ~87% of the ionic conductivity of cold-pressed LPSCl (2.04 mS cm^{-1}). Using lower quantities of binder resulted in brittle sheets with poor mechanical cohesion. Consequently, the same PTFE fraction (0.5 wt.%) was selected for producing the cathode sheets, ensuring comparable behavior during processing.

Regarding the dry-processed cathode, not only high ionic conductivity, but also sufficient electronic conductivity is required, especially at high current densities during cycling [46,47]. Therefore, the partial conductivities were determined by direct current (DC) polarization using symmetric cells with either ion- or electron-blocking electrode configurations, as shown in Fig. 1**c**. For reasons outlined above, cathode sheets containing 0.5 wt.% PTFE were investigated. However, three different formulations were studied. In the following, they are referred to as "uncoated", "coated", and "coated + C65", with their compositions detailed in Fig. 1**d**. In general, additive-free cathodes using either regenerated or $LiNbO_3$-coated NCM85 were compared with those containing the coated CAM and 1 wt.% Super C65 carbon black. Fig. 1**e** shows the room-temperature ionic and electronic partial conductivities of the respective dry-processed sheets. As can be seen, the ionic conductivity increased slightly from $2.8 \bullet 10^{-2}$ mS cm^{-1} for "uncoated" to $4.5 \bullet 10^{-2}$ mS cm^{-1} for "coated". This suggests that the $LiNbO_3$ surface coating likely suppresses chemical side reactions occurring at the CAM|SE interface and thus does not impair ionic conductivity [48]. Cathode composites containing 1 wt.% Super C65 ("coated + C65") exhibited an ionic conductivity of $5.3 \bullet 10^{-2}$ mS cm^{-1}, very similar to the additive-free counterparts. Independent of cathode formulation, the ionic conductivity was found to be lower by about two orders of magnitude relative to the SE separators.

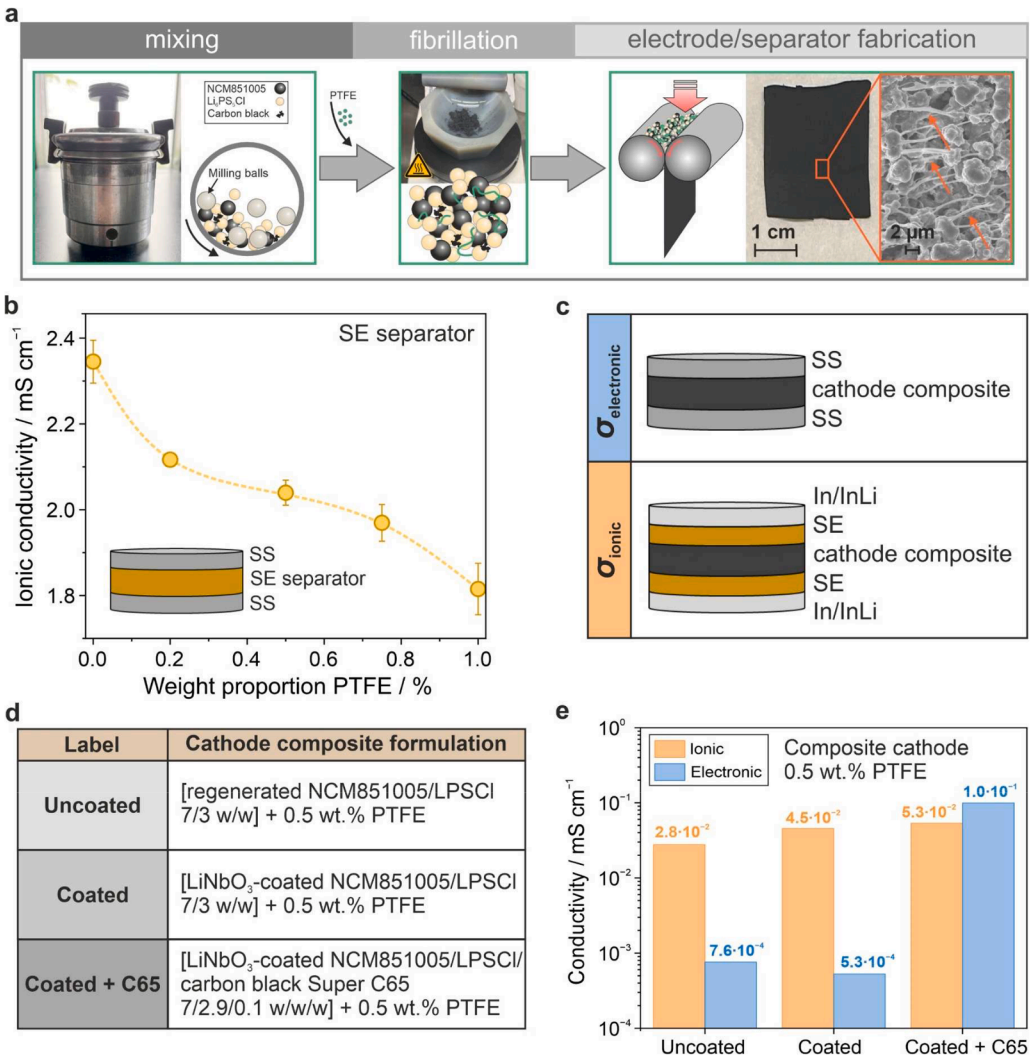

Label	Cathode composite formulation
Uncoated	[regenerated NCM851005/LPSCl 7/3 w/w] + 0.5 wt.% PTFE
Coated	[$LiNbO_3$-coated NCM851005/LPSCl 7/3 w/w] + 0.5 wt.% PTFE
Coated + C65	[$LiNbO_3$-coated NCM851005/LPSCl/ carbon black Super C65 7/2.9/0.1 w/w/w] + 0.5 wt.% PTFE

Fig. 1. Preparation, formulation, and conductivity of the cathode and separator sheets. (a) Schematic representation of the manufacturing process of the cathode, including premixing of materials by ball milling, fibrillation, and sheet preparation. The PTFE fibers present in the composite cathode are highlighted in the SEM image on the right-hand side. (b) Ionic conductivity of separator sheets containing different fractions of PTFE, namely 0%, 0.2%, 0.5%, 0.75%, and 1 wt.%, measured at room temperature. (c) Schematic representation of cell configurations used for determining the electronic and ionic partial conductivities of the cathode sheets. (d) Composition of the formulations tested and (e) ionic and electronic conductivities of the respective cathode sheets with 0.5 wt.% PTFE.

Regarding the electronic partial conductivity of the different cathode sheets, relatively low values of $7.6 \bullet 10^{-4}$ mS cm^{-1} and $5.3 \bullet 10^{-4}$ mS cm^{-1} were determined for "uncoated" and "coated", respectively. However, it increased by three orders of magnitude to $1.0 \bullet 10^{-1}$ mS cm^{-1} for "coated + C65". This improvement is due to facilitated electronic percolation because of the presence of the finely dispersed carbon black additive. Overall, the results demonstrate that the nature of the CAM and the cathode formulation have minor effects on ionic conductivity. However, as expected, the electronic conductivity is strongly increased by adding Super C65 carbon black.

In the context of dry manufacturing, one can assume that carbon black establishes effective point contacts between the CAM and SE particles, but lacks long-range network connectivity. In rigid SSB systems, these contacts tend to break during electrochemical cycling due to volume variations. Fibrous additives such as vapor-grown carbon fibers (VGCFs) or carbon nanotubes (CNTs) could, in principle, bridge larger interparticle distances and further reinforce the electrode, thereby complementing the fibrillar PTFE network. However, since no solvents are used in dry processing, achieving homogeneous fiber dispersions poses a major challenge, as the shear force required for the fibrillation of PTFE and the deagglomeration of VGCFs or CNTs carries the risk of breaking the carbon fibers, thus losing their reinforcing effect. A systematic evaluation of these additive strategies in dry-processed (thiophosphate-based) SSBs represents a promising approach for future research.

After preparation of the dry-processed cathode and separator sheets, their performance in SSBs was evaluated. To systematically assess the influence of cathode and separator processing on cell performance, three distinct configurations were examined, as illustrated in Fig. 2, referred to as "powder-powder", "sheet-powder", and "sheet-sheet" hereafter. Specifically, the "powder-powder" configuration refers to the conventional laboratory-scale approach, sometimes denoted as pelletized cells, where both the cathode and SE separator are cold-pressed into dual-layer pellets and combined with the anode. In the "sheet-powder" configuration, the powder cathode was replaced by a dry-processed sheet, while the separator continued to be produced by cold pressing LPSCl powder. For the "sheet-sheet" configuration, both the cathode and the separator were prepared using the dry process described above (with 0.5 wt.% PTFE). Each cell configuration was further tested with the cathode formulations presented in Fig. 1**d**.

Fig. 3a–c compares the first-cycle charge/discharge curves of the "uncoated", "coated", and "coated + C65" cathode formulations in the

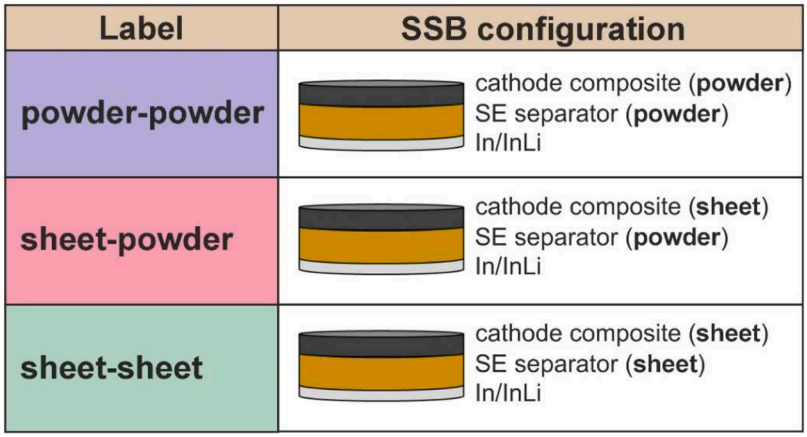

Fig. 2. The different SSB architectures tested in this work (CAM loading: ~13.8 mg_{NCM85} cm^{-2}, SE separator thickness: ~1000 μm).

three different cell configurations at C/10 and at 45°C, with all of them exhibiting characteristic voltage profiles of layered Ni-rich oxide CAMs. In case of the "uncoated" cathode, the "sheet-powder" configuration delivered the highest initial specific discharge capacity of 207 mAh g^{-1}, followed closely by "sheet-sheet" with 204 mAh g^{-1}, while "powder-powder" showed by far the lowest capacity with 183 mAh g^{-1} (see Fig. 3**a**). For the "coated" cathode, the performance gap between the three cell configurations was narrowed (see Fig. 3**b**), with "sheet-sheet" achieving the highest specific discharge capacity of 207 mAh g^{-1}, followed by "sheet-powder" (205 mAh g^{-1}) and "powder-powder" (194 mAh g^{-1}). The addition of carbon black, referring to "coated + C65", further aligned the charge/discharge curves for the different cell configurations (see Fig. 3**c**). As a result, "sheet-sheet" delivered the highest initial specific discharge capacity of 211 mAh g^{-1}, followed by "sheet-powder" (206 mAh g^{-1}) and "powder-powder" (204 mAh g^{-1}). This improvement is likely due to the formation of a continuous electronic percolation network, in addition to mitigated side reactions at the CAM| SE interface provided by the $LiNbO_3$ protective coating.

Besides tracking capacities for the different cathode formulations and cell configurations, the reversibility, expressed by the Coulomb efficiency (CE), is also an important measure for cycling performance. The CEs of the first two cycles at C/10 are given in **Fig. 3d–f**. As can be seen from Fig. 3**d**, for cells using the "uncoated" cathode, the "powder-powder" configuration achieved the lowest initial CE with 82.3%, which was increased to 87.3% and 89.1% for "sheet-powder" and "sheet-sheet", respectively. This indicates that the presence of PTFE alone already has some stabilizing effect, meaning that it helps reduce irreversible side reactions occurring between CAM and SE. In the second cycle, the gap between the different configurations became smaller: the CE increased to 95.9% for "powder-powder", 97.1% for "sheet-powder", and 97.9% for "sheet-sheet".

The first-cycle CE of cells using the "coated" cathode clearly increased for all configurations compared to "uncoated" (see Fig. 3**e**). The "powder-powder" cells offered an initial CE of 92.1%, while "sheet-powder" and "sheet-sheet" achieved 95.3% and 93.1%, respectively. Also, in the second cycle, the CEs increased to 98.8% for the "powder-powder" and "sheet-powder" configurations and to 99.1% for "sheet-sheet". Again, this overall increase in CE can be explained by the presence of a surface coating on the NCM85 particles, thereby partially suppressing detrimental side reactions.

Fig. 3**f** illustrates the CEs of cells using the "coated + C65" cathode. In comparison to "coated", the initial CEs were slightly lower for "powder-powder" (90.7%), "sheet-powder" (91.1%), and "sheet-sheet" (92.1%). The CE in the second cycle was similar for all three configurations (>98%), providing evidence that the carbon additive has only a minor effect on reversibility in the first few cycles.

Fig. 3g–i shows the specific discharge capacities at C/5 over 100 cycles for the different cell configurations and cathode formulations, including rate capability testing at C/10, C/5, C/2, and 1C in the very beginning. The results for cells using the "uncoated" cathode are presented in Fig. 3**g**. Here, "powder-powder" delivered much lower capacities across all tested C-rates compared to the "sheet-powder" and "sheet-sheet" configurations. Regardless, the "powder-powder" cells demonstrated the best stability by showing the least fading, translating to a capacity retention of 88.1%, whereas "sheet-powder" and "sheet-sheet" showed much-reduced values, reaching 79.9% and 82.1% after 100 cycles, respectively (see Fig. 3**j**).

The specific discharge capacities of cells using the "coated" cathode are displayed in Fig. 3**h**, where a similar trend can be seen as for "uncoated". The "powder-powder" configuration delivered the lowest capacities, but the gap between "sheet-powder" and "sheet-sheet" was narrower. However, unlike cells with the "uncoated" cathode, in this case, the "powder-powder" configuration suffered from pronounced fading. By contrast, the "sheet-powder" and "sheet-sheet" configurations delivered higher capacities and were more stable upon cycling operation. This resulted in capacity retentions of 67.5%, 70.3%, and 83.3% for "powder-powder", "sheet-powder", and "sheet-sheet" after 100 cycles, respectively (see Fig. 3**k**).

For the "coated + C65" cathode in the different SSB architectures, the "sheet-sheet" configuration was found to deliver the highest discharge capacities at low C-rates in the beginning of cycling (see Fig. 3**i**), suggesting that the presence of PTFE binder minimizes chemomechanical degradation. However, the corresponding cells experienced the most pronounced fading and achieved the lowest capacity after 100 cycles among the three configurations, corresponding to a capacity retention of only 78.1% (see Fig. 3**l**). Notably, the "sheet-powder" configuration exhibited the best stability (91.9%), followed by "powder-powder" (85.6%). This indicates that both the surface coating and the carbon additive help keep interfacial impedance growth at a minimum and promote more uniform electronic transport throughout the cathode.

Fig. 3**m–o** illustrates the specific discharge capacities achieved with the different cell configurations and cathode formulations in the rate performance test. Fig. 3**m** shows the results for cells using the "uncoated" cathode. Across all C-rates, the "powder-powder" configuration delivered the lowest capacity, reflecting higher interfacial resistance and limited ionic and electronic transport. In contrast, "sheet-powder" and "sheet-sheet" achieved much higher, yet virtually similar capacities, reaching about 140 mAh g^{-1} at 1C. This is indicative of improved particle-particle contact and better CAM utilization in sheet-type cathodes.

Fig. 3**n** compares the rate performance of cells using the "coated" cathode. The protective coating strongly improved the overall discharge capacities compared to the "uncoated" cathode formulation, especially

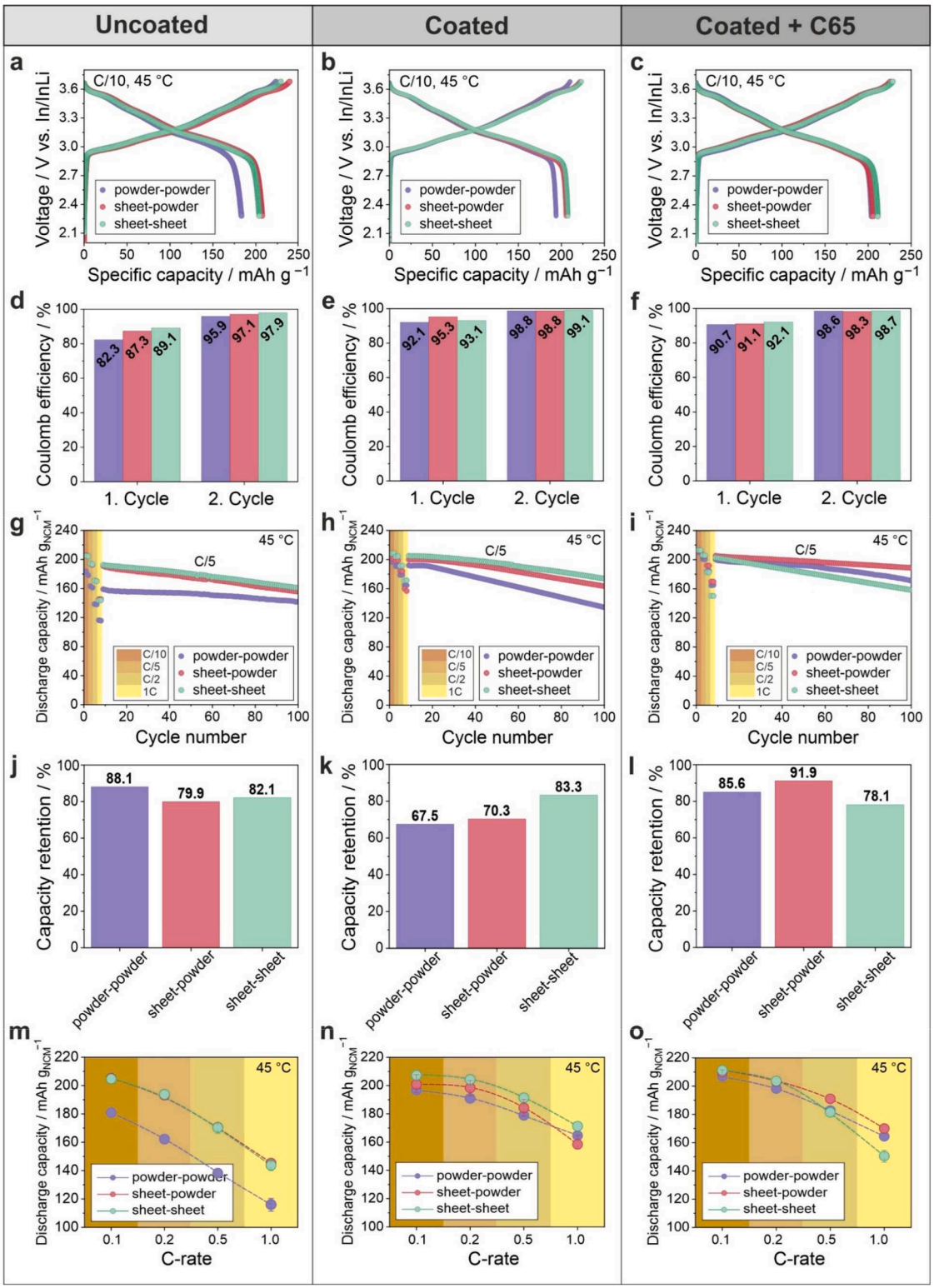

Fig. 3. Electrochemical performance of the different SSB architectures at 45°C: (a, d, g, j, m) "uncoated", (b, e, h, k, n) "coated", and (c, f, i, l, o) "coated + C65". (a–c) Initial voltage profiles at C/10. (d–f) Coulomb efficiencies for the first two cycles at C/10. (g–i) Specific discharge capacities over 100 cycles at C/5. The rate performance test in the beginning is indicated. (j–l) Capacity retentions calculated from the capacities achieved at C/5 in the beginning and at the end of cycling. (m–o) Specific discharge capacities at various C-rates. Data are averaged from at least two identical cells.

at high C-rates, achieving ~171 mAh g^{-1} at 1C for "sheet-sheet". This underscores the beneficial effect of the $LiNbO_3$ surface modification and PTFE binder on suppressing adverse electrochemical and chemo-mechanical processes. In particular, the "sheet-sheet" configuration delivered the highest capacities at all C-rates, again indicating improved particle-particle contact and CAM utilization.

Fig. 3**o** shows the rate capability of the "coated + C65" cathode. Incorporating conductive carbon, in combination with the $LiNbO_3$-coated CAM, increased the specific discharge capacities at low C-rates compared to the other cathode formulations. However, it has a

contradicting effect on rate performance of the different cell configurations. The "sheet-powder" cells revealed the lowest decrease in capacity with increasing C-rate (~170 mAh g^{-1} at 1C). At low C-rates, all configurations exhibited comparable capacities. In contrast, with increasing C-rate, the performance was found to deteriorate more rapidly for "sheet-sheet" and "powder-powder".

As shown in Fig. 3, the highest initial discharge capacities were achieved with the "sheet-sheet" cells, and in terms of rate performance, they also performed best, except for "coated + C65" at C-rates higher than C/2. Likewise, the capacity retention after 100 cycles was improved in most cases; however, it was reduced for "coated + C65" in the "sheet-sheet" cells. This suggests that the carbon additive negatively affects rate capability and cycling stability in sheet-type SSBs. Nevertheless, adding carbon black helps increase the initial capacity, as it improves electronic conductivity and utilization of the active material [49]. However, the interface between the conductive additive and the SE is particularly reactive, accelerating electrochemical degradation of LPSCl, which in turn impairs long-term stability. We hypothesize that in dry-processed cells, improved particle-particle contact in the cathode leads to an increase in interfacial area, thereby triggering unwanted side reactions. In addition, the interface between anode and separator is critical in PTFE-containing SSBs. It is known that while PTFE is stable toward electrochemical oxidation, it is readily reduced at low potentials according to:[50–52]

$$6(CF_2) + 12\,Li^+ + 12\,e^- \rightarrow C_6 + 12\,LiF \quad (1)$$

Ultimately, this leads to the formation of insulating LiF and amorphous carbon, with the latter providing additional electronic percolation paths, thus further accelerating SE decomposition. This kind of degradation is evident from the impedance evolution of Li|SE|Li cells shown in **Figure S1** (Supporting Information). Specifically, both SE powder as well as sheets containing 0.5 wt.% PTFE were examined. As can be seen, the resistance increase was larger for the PTFE-containing separator, in line with expectations. Overall, it can be assumed that during cycling, cells using the separator sheet experience degradation of the PTFE and thus of the SE, leading to a continuous loss of capacity. Therefore, the "sheet-sheet" cells exhibit a relatively lower long-term stability than the "sheet-powder" and "powder-powder" configurations. Aside from this (electrochemically-driven) negative effect of PTFE on stability, the mitigation of detrimental chemomechanical effects positively contributes to cyclability, which might explain the better performance of the sheet-type SSBs in the beginning of cycling.

To track microstructural changes occurring in the cathode upon cycling, *post mortem* SEM imaging of ion-polished cross-sections was performed. **Fig. 4a–c** shows images at different magnifications of the "coated" cathode harvested from "sheet-sheet" cells in the pristine state and after 50 and 100 cycles at C/5. The pristine cathode was characterized by a relatively open microstructure with loosely packed NCM85 secondary particles and interparticle voids, despite compaction during cathode preparation (see Fig. 4**a**). After 50 cycles, the cracks in the NCM85 particles and between CAM and SE increased slightly, indicating stress accumulation (see Fig. 4**b**). In general, the NCM85 retained its spherical morphology and showed no major signs of fracturing. After 100 cycles, crack propagation intensified, accompanied by the beginning of interfacial detachment and coalescence of pores into larger voids within the SE matrix, leading to a gradual loss of structural integrity (see Fig. 4**c**). Regardless, the dry-processed (sheet-type) cathode delivered higher capacities and showed better stability than their pelletized counterpart (carbon-additive-free case). This is likely due to the mechanically more flexible structure of the PTFE-containing cathode, which allows for better accommodation of volume changes. We also assume that the existing porosity acts as a buffer zone, reducing stress build-up at the macroscopic level and promoting maintenance of intimate particle-particle contact. The superior performance of the sheet-type cathode is therefore primarily due to improved contact between the particles—facilitated by PTFE—and the resulting mechanical integrity, rather than to a higher packing density. In fact, while the powder cathodes compacted at 437 MPa exhibit a higher density, they

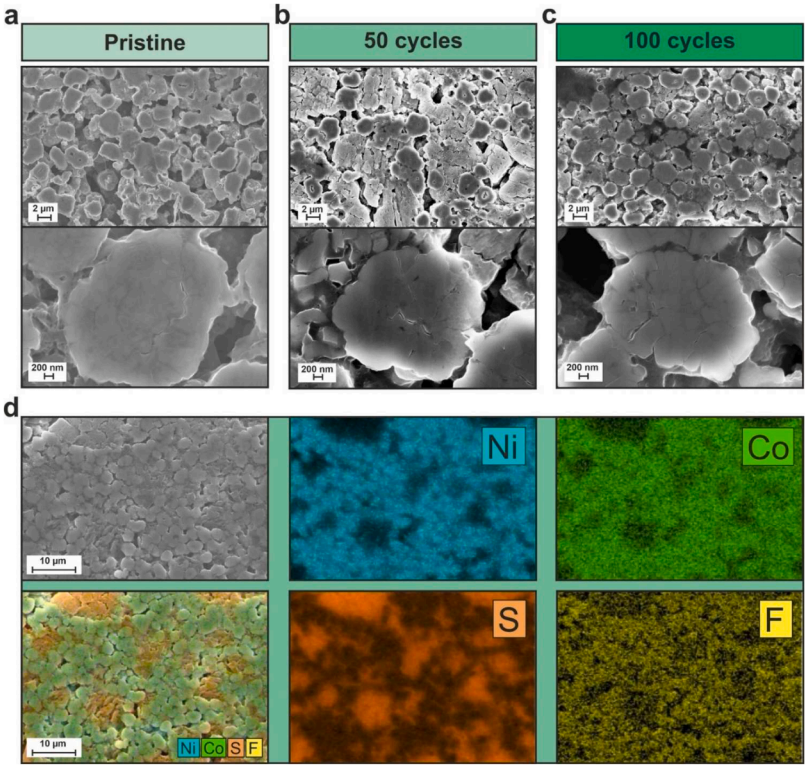

Fig. 4. Low- and high-magnification cross-sectional SEM images of the "coated" cathode ("sheet-sheet" cell configuration) taken (a) before cycling and (b) after 50 and (c) 100 cycles at C/5. (d) Corresponding SEM-EDX analysis after 50 cycles with individual elemental maps and an overlay image.

consistently demonstrate poorer cyclability. However, quantification of the pore structure *in situ* is very difficult and has not yet been performed. In contrast, pelletized cathodes and SE separators are less tolerant to chemomechanical degradation and tend to fracture, resulting in increased interfacial resistance and accelerated capacity decay. In this regard, it should be noted that in the SSBs tested in this work, In/InLi served as the anode. During (de)lithiation, the alloy anode undergoes major volume changes, which are significantly larger than those of the cathode. Consequently, the pressure evolution in such cells is primarily determined by the expansion and contraction of the anode,[53] which is likely somewhat mitigated by the fibrillar PTFE network and the residual porosity. Regardless, the ability to "absorb" pressure depends crucially on the cathode architecture, with the flexible network in the sheet-type cathode apparently distributing the load more effectively, whereas the (brittle) pelletized cathode is more prone to cracking under similar conditions.

The sustained microstructural integrity of the sheet-type cathode is also evident from the cross-sectional SEM image and corresponding elemental maps from energy dispersive X-ray (EDX) spectroscopy in Fig. 4**d**. There were no signs of major cracking within individual particles and, more importantly, in the cathode sheet as a whole. This stands in stark contrast to previous observations with pelletized cathodes made from similar materials [54–56].

The systematic experimental design of this study allows for a meaningful assessment of the influence of chemomechanical integrity on cell performance. Since the separator is identical in the "sheet-powder" and "powder-powder" cells, any performance differences between these two configurations are directly related to the cathode architecture. The consistently lower electrochemical performance of the pelletized cathode, despite its higher packing density, suggests that density and interfacial contact alone are not decisive for cycling stability; rather, the mechanical integrity ensured by PTFE is the decisive factor.

To characterize decomposition products in the composite cathodes, time-of-flight secondary ion mass spectrometry (ToF-SIMS)

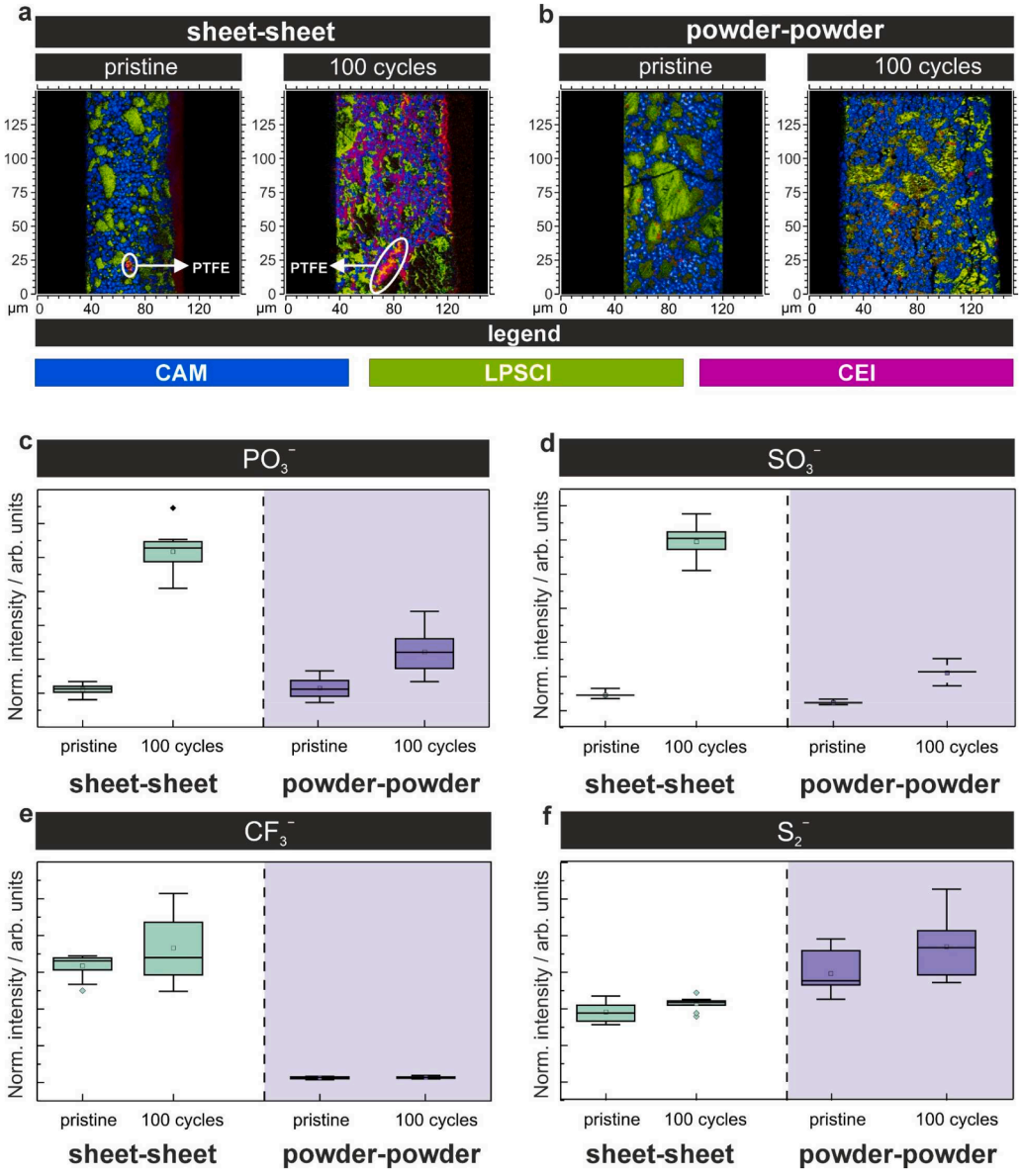

Fig. 5. ToF-SIMS results for the "coated" cathode in the "sheet-sheet" and "powder-powder" cell configurations before and after cycling. (a, b) Images representing overlay ion maps of the NiO^-, NiO_2^-, MnO_2^-, and CoO_2^- fragments (blue, indicating the CAM), as well as of the PS^-, PS_2^-, and PS_3^- fragments (green, indicating the SE) and the PO^-, PO_2^-, and PO_3^- fragments (pink, indicating the CEI). Corresponding box plots of the normalized intensities of (c) PO_3^-, (d) SO_3^-, (e) CF_3^-, and (f) S_2^- fragments.

measurements were performed. ToF-SIMS enables detailed investigation of chemical degradation processes by identifying fragments related to SE decomposition, such as the formation of sulfate and/or phosphate species [57]. To assess the influence of PTFE on cathode degradation, the "coated" cathode in the "sheet-sheet" and "powder-powder" configurations was analyzed in its pristine state and after 100 cycles at C/5. In Fig. 5**a** and **b**, secondary ion images of the pristine and cycled cathodes are shown as overlay maps of negatively charged ion fragments. In the pristine state, both cathode types exhibited a predominant coexistence of CAM-dominated regions (blue) and SE-dominated regions (green). However, weak signals related to PO_x^- ($1 \leq x \leq 3$, pink) were also detected, indicating decomposition of the SE and resulting in the formation of a cathode electrolyte interphase (CEI). Previous studies have demonstrated that small amounts of oxygenated phosphorus species can already form upon physical contact between NCM CAMs and thiophosphate SEs [49,58]. Despite the similarities between the sheet-type and pelletized cathodes, distinct morphological differences were evident in the pristine state. The sheet-type cathode (see Fig. 5**a**) exhibited smaller and more uniformly distributed SE particles, whereas the pelletized cathode (see Fig. 5**b**) revealed a more heterogeneous, granular morphology with relatively larger SE particles. This is likely related to the manufacturing process. In particular, the additional step necessary to achieve PTFE fibrillation during preparation of the dry-processed cathode apparently leads to further fragmentation, i.e., size reduction of large (>20 μm) LPSCl particles and/or agglomerates. After 100 cycles, the sheet-type cathode exhibited an increased concentration of PO_x^- fragments (pink) distributed around the CAM particles, representing the growing CEI (see Fig. 5**a**). As can be seen, this decomposition layer forms an interconnected network that is not limited to individual contact points between CAM and SE, but extends throughout the cathode. In addition, CF_3 fragments were detected, which can be attributed to the PTFE fibers. Note that the PTFE-containing areas are barely visible, as the finely fibrillated fibers cannot be resolved by ToF-SIMS due to their small diameter (in the nanometer range), as well as the limited lateral resolution of the technique. In contrast, the pelletized cathode largely retained its original microstructure after cycling (see Fig. 5**b**). Although CEI-related signals increased in intensity, they appear less spatially extended and are more strongly confined to local contact areas compared to the sheet-type cathode. Overall, the pelletized cathode was less dominated by ion fragments related to the CEI.

The box plots in **Fig. 5c–f** show the evolution of the normalized intensities of PO_3^-, SO_3^-, CF_3^-, and S_2^- fragments for the sheet-type and pelletized cathodes before and after cycling. These fragments serve as markers for different degradation and aging processes. The PO_3^- fragment is an indicator of oxygenated phosphorus species (Li_3PO_4 and/or transition metal phosphates) and its increase in intensity directly reflects the CEI formation. Detection of these species requires decomposition of the thiophosphate SE in the presence of oxygen, which may be released from the CAM at high degrees of delithiation. The SO_3^- fragment is clearly associated with anodic SE degradation and represent the formation of Li_2SO_4 or other oxidized sulfur species (typically arising from interfacial oxidation of S^{2-} species in the presence of oxygen during cycling) [58]. The CF_3^- fragment originates from fluorocarbon species and can be attributed to the PTFE [59]. The S_2^- fragment is associated with sulfur species originating from the electrochemical decomposition of the SE and indicates the presence of polysulfides [60].

The box plot in Fig. 5**c** reveals an increase in PO_3^- intensity after cycling for both cathode types compared to their pristine state. However, this increase is much more pronounced for the sheet-type cathode, indicating stronger SE degradation during SSB operation. In the pristine state, both cell configurations exhibited similarly low PO_3^- intensities, suggesting limited (initial) interfacial reactivity. After cycling, the intensity distribution in the sheet-type cathode shifted markedly toward higher values, evidencing increased formation of phosphate-containing CEI components compared to the pelletized cathode. Analogous to PO_3^-, the SO_3^- fragment also showed a significant increase in intensity after 100 cycles, particularly for the sheet-type cathode (see Fig. 5**d**). Previous studies have demonstrated that sulfates and sulfites frequently coexist with phosphates and dominate the CEI composition [58]. The CF_3^- fragment was naturally observed only in the sheet-type cathode (see Fig. 5**e**). The respective signal was already detected in the pristine state and increased in intensity upon cycling. However, the relative increase was small compared to that of PO_3^- and SO_3^-, which suggests that there is no significant degradation of the binder. PTFE is relatively inert within the relevant potential window (cathode), and the observed minor changes in CF_3^- signal are more plausibly explained by mechanical effects, such as fibrillation or local accumulation, rather than electrochemical decomposition.

In contrast to the PO_3^- and SO_3^- fragments, the S_2^- box plots only show moderate changes between the pristine and cycled states (see Fig. 5**f**). Notably, the pelletized cathode exhibited overall higher intensities than the sheet-type cathode, particularly after 100 cycles. This observation suggests that polysulfide formation may be more pronounced in the pelletized cathode. Such degradation pathways have been associated with locally increased electronic conductivity or ill-defined contact conditions in composite cathodes, which can promote partial polysulfide formation from thiophosphate SEs [49]. At the same time, the relatively small increase in S_2^- intensity indicates that polysulfide formation plays a secondary role. Overall, the results suggest that electrochemically-induced cathode degradation is clearly oxidative in nature, with polysulfides and related species representing locally confined decomposition products and are predominantly present in the pelletized cathode.

In summary, the sheet-type cathode exhibited more severe interfacial degradation, particularly in the form of oxygenated phosphorus- and sulfur-containing species. Nevertheless, as shown in Fig. 3**h**, the sheet-type cells outperformed the pelletized cells in terms of initial capacity and capacity retention. This apparent discrepancy underscores that chemical and electrochemical degradation of the SE alone is not the dominant factor governing performance. Rather, the experimental data suggest that mechanical integrity, which is significantly improved in the sheet-type cathode due to the usage of PTFE, is of greater importance. The CEI formation appears to be acceptable as long as the mechanical integrity and contact between the particles within the cathode are maintained. In contrast, the overall lower degree of electrochemical degradation in the pelletized cathode does not translate into improved performance, as mechanically-induced contact loss (interfacial delamination) and structural instabilities likely dominate. It can therefore be assumed that, in the case of thiophosphate-based SSBs, long-term cyclability is determined more by chemomechanics than by electrolyte degradation, as had already been suspected in the past [55]. This conclusion is based on consistent findings from multiple observations: higher initial capacities and better rate capability despite more pronounced degradation effects (ToF-SIMS), preserved microstructural integrity (SEM), and the particularly clear result for the additive-free "coated" formulation (83.3% vs. 67.5% capacity retention for "sheet--sheet" and "powder-powder", respectively, after 100 cycles).

Using ToF-SIMS, only the solid decomposition products forming in the sheet-type and pelletized cathodes upon cycling were examined. However, it is known that gaseous species can also be produced during SSB operation, which directly affects cell degradation [61]. Hence, differential electrochemical mass spectrometry (DEMS) measurements were performed at C/20. The low C-rate was chosen to enable access to specific capacities representing reasonable states of charge, since only a negligible stack pressure can be applied to the cells in the DEMS setup. The "powder-powder" cells achieved initial specific charge and discharge capacities of 226 mAh g^{-1} and 178 mAh g^{-1}, respectively, corresponding to a first-cycle CE of 78.8%. For the "sheet-sheet" cells, the respective values were 217 mAh g^{-1} and 172 mAh g^{-1} (79.3% CE). The achieved states of charge were about 82% for "powder-powder" and 79% for "sheet-sheet". Note that the "powder-powder" cells were cycled

between 2.3 V and 3.9 V vs. In/InLi (equivalent to ~2.9–4.5 V vs. Li^+/Li), while the "sheet-sheet" cells were cycled between 2.3 V and 4.4 V vs. In/InLi (~2.9–5.0 V vs. Li^+/Li). The extended voltage window of the latter cells was necessary to achieve similar states of charge.

The mass fragments corresponding to hydrogen ($m/z = 2$), oxygen ($m/z = 32$), carbon dioxide ($m/z = 44$), and sulfur dioxide ($m/z = 64$) were continuously monitored and compared for both cell types. Fig. 6**a** and **b** displays the respective gas evolution traces together with the voltage profiles. Overall, the "powder-powder" cells were found to release lower cumulative amounts of gases, except for SO_2. The total evolved quantities of H_2 were ~5.8 µmol g_{NCM85}^{-1} for "powder-powder" and 8.1 µmol g_{NCM85}^{-1} for "sheet-sheet". The detection of hydrogen at the onset of the first charge is commonly observed in DEMS studies on SSBs and is generally attributed to the electrochemical reduction of trace water or surface hydroxyl species within the SE or at the electrode interfaces. These protic impurities are reduced to H_2 during the initial polarization of the cell, leading to the appearance of a sharp hydrogen signal at the beginning of cycling [61]. The most pronounced difference was observed for O_2, with ~10 µmol g_{NCM85}^{-1} for "powder-powder", compared to ~24 µmol g_{NCM85}^{-1} for the "sheet-sheet" cells. O_2 was detected near the end of charge, starting around 3.7 V vs. In/InLi, consistent with the onset of the H2-H3 phase transition, where lattice oxygen becomes unstable and is partially released from the NCM85 [62]. The CO_2 evolution amounted to ~5.8 µmol g_{NCM85}^{-1} for "powder--powder" and ~7.1 µmol g_{NCM85}^{-1} for "sheet-sheet". CO_2 release occurred at potentials similar to those observed for O_2, suggesting its origin from the oxidative decomposition of surface carbonates (e.g., Li_2CO_3). The smaller difference between the two cell configurations for the cumulative amount of released carbon dioxide as compared to oxygen suggests that its formation is predominantly surface-limited, rather than strongly voltage-dependent, in agreement with prior DEMS investigations into layered Ni-rich oxides [63].

Interestingly, SO_2 was only detected in the "powder-powder" cells, evolving in the same potential range as oxygen. This observation agrees with the assumption of secondary reactions between the released lattice oxygen and the thiophosphate SE, yielding SO_2 as a gaseous byproduct [61,64]. Since SO_2 could not be quantified, its evolution can only be discussed qualitatively based on measured ion currents. The absence of detectable SO_2 in the "sheet-sheet" cells, despite the more pronounced O_2 evolution, may be attributed to differences in gas diffusion pathways or altered interfacial contact between CAM and SE, which apparently affects gas-solid interactions and limits SO_2 release. This is in agreement with the ToF-SIMS results, indicating the formation of oxygenated phosphorus and sulfur species (see Fig. 5). Furthermore, the overall higher outgassing of O_2 and CO_2 in the "sheet-sheet" cells is likely due to the higher upper cutoff potential. It is important to note that the outgassing of NCM-type CAMs depends primarily on the degree of delithiation, i.e., on the state of charge (SOC), whereby oxygen release—as has been established in the literature—typically begins at ~80%, regardless of the voltage window [62,65]. Since both cell configurations achieved very similar SOC values of (79–82)%, the DEMS data are compared on an appropriate basis. In addition, **Figure S2** shows how gas evolution depends on the potential [62].

To assess the performance of the cells in the context of existing literature, Fig. 7**a** shows the specific discharge capacity and initial CE for various SSBs manufactured by dry processing [34,36,40,41,66–70]. However, the cells reported in the literature differ in terms of key parameters, such as C-rate, cathode chemistry, anode type, fabrication and/or stack pressure, and operating temperature. All relevant information for the individual data points is summarized in the Supporting Information (see **Table S1**). As is evident, the sheet-type cathodes based on $LiNbO_3$-coated NCM85 and 1 wt.% Super C65 reported in this work achieve a very promising combination of high capacity and reversibility among the dry-processed SSBs described so far, particularly given that both cathode and separator were manufactured using a dry process and no additional compaction step was performed during cell assembly. They achieved an excellent initial specific discharge capacity of 211 mAh g^{-1} and a CE of 92.1% (see Fig. 7**a**, green star). Only one cell reported by Lee *et al.*[69] achieved a higher initial CE of 95%, but with a significantly lower specific discharge capacity of 169 mAh g^{-1} and was

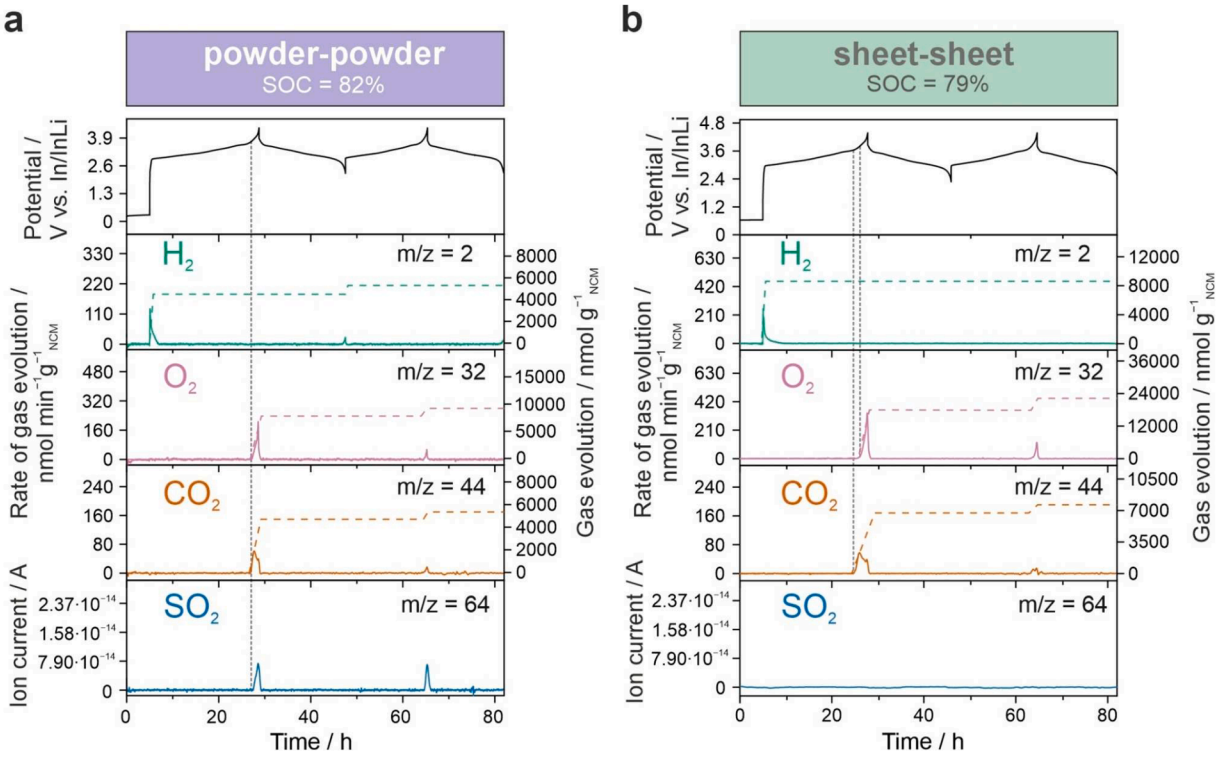

Fig. 6. *In situ* gas analysis of the "coated" cathode in the "powder-powder" and "sheet-sheet" cell configurations. (a, b) First- and second-cycle voltage profiles at C/20 and 25°C, as well as the time-resolved evolution rates and cumulative amounts for H_2, O_2, CO_2, and SO_2.

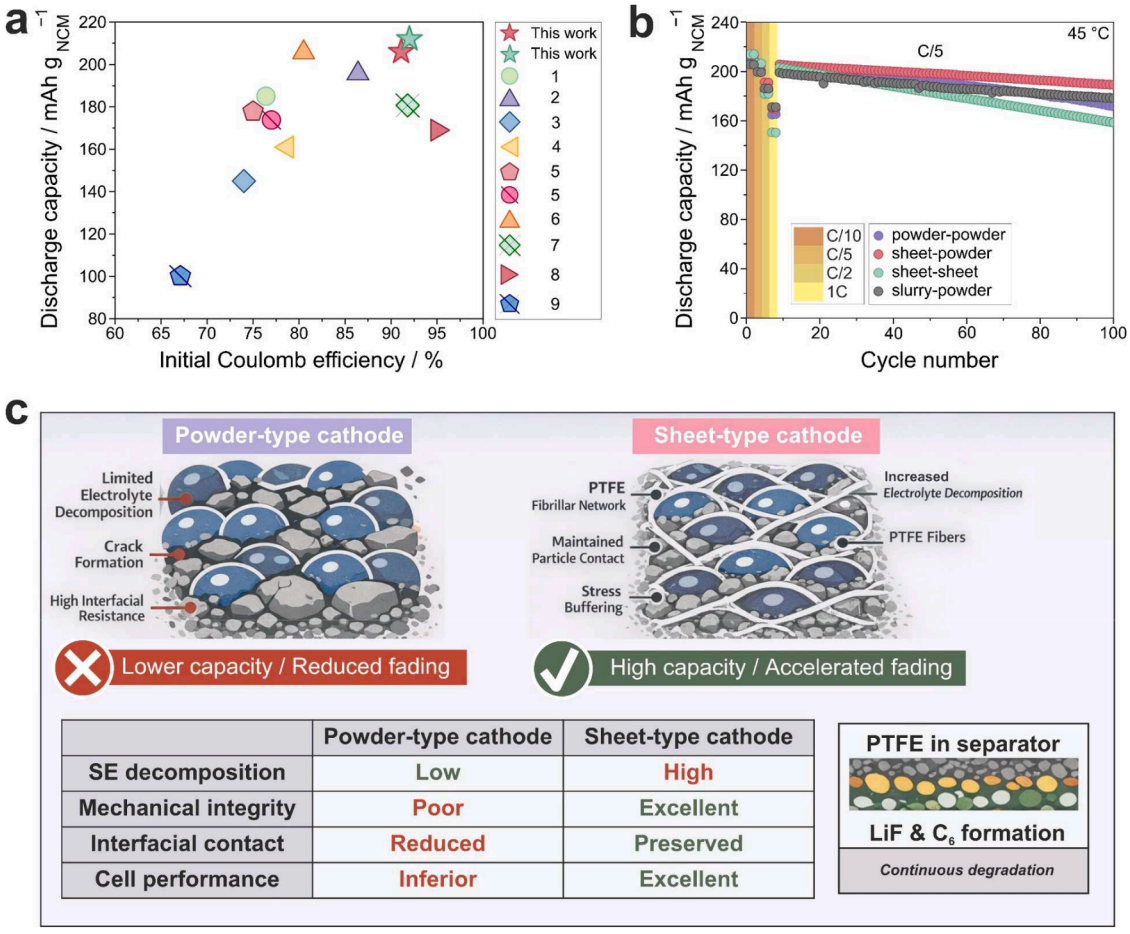

Fig. 7. (a) Comparison of the first-cycle specific discharge capacity and initial Coulomb efficiency of dry-processed SSB cells, based on data from the literature and our own work (denoted as stars). The respective references are given in **Table S1** (Supporting Information). (b) Comparison of cycling performances of the "coated + C65" cathode in various dry- and wet-processed cell configurations. First-cycle Coulomb efficiencies at C/10: "sheet-powder" 91.1% (red) and "sheet-sheet" 92.1% (green). (c) Schematic representation of the different processes affecting the cyclability of SSBs with pelletized or sheet-type cathode.

tested at a higher temperature of 60°C instead of 45°C. A key difference from most literature cells is that both the cathode and the separator in the respective cell configurations described herein were manufactured using a dry process. The vast majority of published systems use exclusively a dry-processed cathode, whereas the SE separator is typically a pellet pressed from powder, which offers advantages due to its higher density and better ionic conductivity. For that reason, we have also included the data point for such a cell configuration in Fig. 7**a** (red star) for comparison, delivering a first-cycle specific discharge capacity of 206 mAh g^{-1} and an initial CE of 91.1%. It should also be noted that the "sheet-sheet" cells were produced without any additional compression step during manufacturing and therefore likely contain a higher degree of residual porosity. Furthermore, some studies use customized binder strategies, such as Nafion instead of PTFE (Cha *et al.*),[66] cryogenic pulverization to improve PTFE distribution (Lee *et al.*),[67] or ion-conducting ionomers (Hong *et al.*) [68]. Nevertheless, the cells tested in this study outperform these approaches, and the combination of high capacity, high CE, and completely dry manufacturing emphasizes their exceptional cyclability.

In addition, the performance of the dry-processed cells using the "coated + C65" cathode in the "powder-powder", "sheet-powder", and "sheet-sheet" configurations is compared to that of a slurry-cast cathode tested in "sheet-powder" cells (using the same materials and fabricated according to the method described by *Ma et al.*) (see Fig. 7**b**) [71,72]. In the beginning of cycling at low C-rates (C/10 and C/5), the "sheet-sheet" cells achieved the highest discharge capacities, while the slurry-cast cells delivered the lowest ones. However, with increasing C-rate, this trend reversed and the cells with the slurry-cast cathode achieved the highest capacities at 1C. For the dry-processed cells, the long-term cycling performance is shown in Fig. 3. The slurry-cast cathode achieved a capacity retention of 89.0% after 100 cycles, which is equivalent to the best performance of the cells shown in Fig. 7**b** and is comparable to the dry-processed "sheet-powder" cells (91.9% capacity retention). This comparison confirms that tailoring the manufacturing process, particularly through the use of a polymer binder, helps improve the cyclability, especially in terms of capacity retention. To illustrate this, Fig. 7**c** shows the different electrochemical and chemomechanical processes at play that dictate the performance of the pelletized and sheet-type SSBs.

Overall, the better performance of the sheet-type cathodes can be ascribed to superior mechanical integrity. However, if PTFE is present in the SE separator, continuous electrochemical degradation occurs, which negatively affects long-term stability, as described in detail before. In summary, our work not only demonstrates a significant performance improvement over dry-processed SSB cells reported in the literature, but also shows that such cathodes are competitive or even superior to slurry-cast systems. This underscores the great potential of the proposed approach for scalable next-generation electrode concepts.

3. Conclusions

In summary, this work provides a comprehensive assessment of dry-processed cathode and separator sheets for solid-state batteries (SSBs) and highlights the complex interplay between electrochemical and

chemomechanical degradation processes. In particular, the cycling performance of various cell configurations was investigated, in which a fibrillated polytetrafluoroethylene (PTFE) binder was incorporated either only into the cathode or into both the cathode and the separator, and these were compared to pelletized variants produced by cold pressing. The introduction of PTFE is shown to fundamentally alter the cathode's microstructure, particle-particle contacts, and mechanical compliance, all of which has a strong effect on cell performance. Compared to their pelletized counterparts, such sheet-type cathodes consistently exhibited higher initial specific discharge capacities, improved rate capability, and superior Coulomb efficiency. While a $LiNbO_3$ protective coating on the cathode active material effectively suppressed adverse side reactions and conductive carbon black improved electronic percolation, the presence of the aforementioned additive in combination with PTFE accelerated interfacial degradation.

Post mortem analyses revealed that the sheet-type cathodes exhibit more pronounced SE decomposition and gas evolution; however, this kind of degradation is offset by their higher mechanical stability. The results clearly show that, in thiophosphate-based SSBs, maintaining mechanical integrity is more critical to long-term performance than minimizing SE decomposition. At the same time, PTFE-containing separator sheets lead to additional degradation pathways, thus underscoring an important limitation of current dry-processing strategies. Overall, this study confirms that dry manufacturing is an efficient and scalable method for practical SSBs while also identifying key material and structural parameters that need to be optimized to fully realize the potential for widespread application.

The mechanical assessment in this study is based on indirect evidence from SEM imaging and electrochemical testing. In this regard, direct micro- or nanomechanical characterization would be extremely beneficial; however, from an experimental perspective, it would be very difficult due to the residual porosity present in the cells.

4. Experimental Section

General. If not stated otherwise, all materials were handled and procedures were carried out in an argon glovebox with water and oxygen levels maintained below 0.5 ppm. Super C65 carbon black (TIMCAL Ltd.) was dried under dynamic vacuum (10^{-3} mbar) overnight before use.

Surface coating. The $LiNi_{0.85}Co_{0.1}Mn_{0.05}O_2$ (NCM85, BASF SE) was first heated for 3 h at 750°C under oxygen flow, with heating and cooling rates set to 5°C min^{-1}, to remove residual lithium present on the free surface (labeled as "regenerated" herein). To apply a 1 wt.% $LiNbO_3$ coating, stoichiometric amounts of lithium ethoxide (1 M) and niobium ethoxide solutions (0.5 M) were added to the NCM85. The mixture was blended via ultrasonication for 30 min before the solvent was removed by vacuum treatment. Subsequently, the powder was heated for 2 h at 350°C under oxygen flow.

Dry processing of cathode and solid-electrolyte separator sheets. For the preparation of dry-processed cathodes, three different powder mixtures were used. Composite (1) consisted of 70 wt.% regenerated NCM85 and 30 wt.% Li_6PS_5Cl (LPSCl, NEI Corp.). For composite (2), $LiNbO_3$-coated NCM85 was used. Composite (3) contained $LiNbO_3$-coated NCM85, LPSCl, and Super C65 in a weight ratio of 70:29:1. Each cathode composite was produced by ball milling for 30 min at 140 rpm. To this end, 70 mL zirconia jars together with 10 zirconia balls of 10 mm diameter were used, and the total mass of the composite was 1 g. Subsequently, it was transferred to a preheated mortar at 80°C and 0.5 wt.% polytetrafluorethylene (PTFE, Goodfellow GmbH, $d_{50} = 675$ μm) was added. The mixture was manually ground for ~20 min until PTFE fibrillation occurred and a single cathode composite flake was formed. This flake was then placed on a glass plate, followed by roll out using a glass cylinder until the desired thickness was achieved (~120 μm). Next, the electrode sheets were compacted at a line pressure of 3 N mm^{-1} in a dry room atmosphere with dew point below −50°C using a roll press (Sumet Messtechnik). Finally, cathode discs with a diameter of either 9 or 10 mm were punched out.

Solid-electrolyte sheets were prepared by directly adding 0.5 wt.% PTFE to LPSCl in a preheated mortar at 80°C. Separator discs with a diameter of 10 mm and thickness of ~1000 μm were obtained according to the processing steps described above.

Wet processing of cathode sheets. For the preparation of slurry-cast cathodes, an *o*-xylene-based slurry containing $LiNbO_3$-coated NCM85, LPSCl, Super C65, and OPPANOL N 150 polyisobutylene binder (BASF SE) in a weight ratio of 68.6:29.4:1.0:1.0 was spread onto aluminum foil, followed by first natural drying and then vacuum-drying overnight at room temperature [69,70].

Conductivity measurements. For the measurement of ionic conductivity of the solid-electrolyte separator, either pure LPSCl powder or sheets containing different fractions of PTFE were placed in a PEEK sleeve (10 mm inner diameter). Stainless-steel (SS) plates were positioned on both sides to ensure uniform contact. Electrochemical impedance spectroscopy (EIS) was then carried out in the frequency range from 0.1 Hz to 7 MHz, with a 20 mV voltage amplitude and with an external pressure of 200 MPa, using a BioLogic SP-200 potentiostat.

The electronic and ionic partial conductivities of the cathode sheets were measured by direct current (DC) polarization. To this end, the cathode discs were placed in a symmetric cell configuration under a stack pressure of 200 MPa. To determine the electronic conductivity, an ion-blocking configuration of type SS|cathode sheet|SS was used, and a DC voltage of 50 mV was applied. The response was monitored until a steady-state current was reached. To determine the ionic conductivity, an electron-blocking configuration of type In/InLi|solid-electrolyte sheet|cathode sheet|solid-electrolyte sheet|In/InLi was used, and a DC voltage of 100 mV was applied at room temperature (indium foil: 9 mm diameter and 125 μm thickness, Thermo Fisher Scientific; lithium foil: 6 mm diameter and 50 μm thickness, Albemarle Corp.; solid-electrolyte sheet: 0.5 wt.% PTFE, 10 mm diameter; cathode sheet: 0.5 wt.% PTFE, 10 mm diameter). Measurements were performed using a BioLogic SP-200 potentiostat, and conductivities were calculated from the steady-state current under consideration of the electrode area, sample thickness, and applied voltage.

All conductivity measurements were performed at room temperature.

Cell assembly and electrochemical testing. A customized cell setup with SS current collectors and a PEEK sleeve (10 mm inner diameter) was used for cell assembly. The cathode composites were electrochemically tested in three different SSB configurations, denoted as "pellet-pellet", "sheet-pellet", and "sheet-sheet". For assembling the "pellet-pellet" cells, 100 mg of LPSCl was first compressed at 62 MPa to produce the separator. The cathode composite powder was then evenly distributed on one side of the separator, and the stack was compressed at 437 MPa. Finally, an In/InLi anode (for details, see above) was placed on the other side of the separator, with the indium foil facing the separator layer. For the "pellet-sheet" cells, the powder was replaced by a cathode sheet (9 mm diameter), and the procedure was similar to the one described before. In case of the "sheet-sheet" cells, the cathode sheet (9 mm diameter), the solid-electrolyte separator sheet (10 mm diameter), and the In/InLi anode (for details, see above) were sequentially stacked without additional pressing.

Galvanostatic charge/discharge measurements were performed after 1 h open circuit voltage (OCV) rest at different rates of C/10, C/5, C/2, and 1C, with 1C = 190 mA g^{-1}, and at 45°C and 81 MPa (external stack pressure) using a MACCOR battery cycler. The potential window was set to 2.3–3.7 V vs. In/InLi (approx. 2.9–4.3 V vs. Li^+/Li).

Ion polishing and scanning electron microscopy. SEM analysis was performed at an accelerating voltage of 10 kV using a LEO-1530 microscope (Carl Zeiss AG) with a field emission source. For cross-sectional imaging, an IB-19510CP polisher (JEOL Ltd.) with an argon-gas source was employed.

Differential electrochemical mass spectrometry. For the DEMS

measurements, cells were prepared in a manner similar to those used for electrochemical testing, with the exception that only indium metal served as the anode. They were assembled in a 10 mm diameter PEEK ring by sequentially pressing the individual components into a pellet before transferring them into the DEMS setup. Galvanostatic cycling was performed at room temperature and at a rate of C/20 within potential windows of 2.3–3.9 V vs. In/InLi for the "powder-powder" cells and 2.3–4.4 V vs. In/InLi for the "sheet-sheet" cells, corresponding to approx. 2.9–4.5 V and 2.9–5.0 V vs. Li^+/Li, respectively, using a Bio-Logic VSP-300 potentiostat. To ensure temperature equilibrium and a stable background, all cells were held for 6 h at OCV prior to cycling. The helium carrier-gas flow (2.5 mL min^{-1}, 6.0 purity) was regulated by a mass flow controller (F-201CV-020-RAD-33-Z, Bronkhorst). The outgassing behavior was analyzed using a quadrupole mass spectrometer (OmniStar GSD 320 O, Pfeiffer Vacuum GmbH).

Time-of-flight secondary ion mass spectrometry. Sample transfer to the ToF-SIMS instrument was achieved under inert conditions using an VCT500 vacuum-cryo-transfer system (Leica Microsystems, Germany), thus preventing degradation due to contact with ambient atmosphere. ToF-SIMS studies were carried out on an M6 Plus from IONTOF GmbH. The instrument is equipped with a bismuth liquid metal ion gun (LMIG, nanoprobe 50) for analysis. All measurements, including surface analysis and 2D imaging, were performed in negative polarity using Bi_3^{++} primary ions with an energy of 60 keV. Surface spectra were recorded in spectrometry mode [bunched mode, full width at half maximum (FWHM) of $m/\Delta m = 9616@m/z$ 48.00 (S_2^-)], providing a high signal intensity, and were combined with the high mass resolution setting of the analyzer. The raster size was 200 μm × 200 μm, with a pixel number of 128 × 128 and a total ion dose of $1.0 \bullet 10^{-12}$ cm^{-2}. For each sample, 10 different spots were measured to increase statistics. The primary ion current was 0.19 pA, with 100 μs duty cycle. For surface imaging, the fast-imaging mode [unbunched mode, FWHM of $m/\Delta m = 8324@m/z = 48.00$ (NiO_2^-)] was used in combination with the delayed extraction analyzer setting to allow 2D studies of the chemical distribution in the cathode cross-sections. The analysis area was 150 μm × 150 μm, and the surface was rasterized with 1024 × 1024 pixels. The primary ion current was about 0.014 pA, with a cycle time of 100 μs. The composite cathodes were first broken manually and then ion milled at −100°C under vacuum using a triple ion beam cutter (EM TIC 3X, Leica Microsystems, Germany), equipped with three argon-ion guns. The operating conditions involved 7 kV, ~2.5 mA, and a polishing time of 7 h.

Declaration of competing interest

The authors declare that they have no known competing financial interests or personal relationships that could have appeared to influence the work reported in this paper.

Acknowledgements

M.S and F.S. are grateful to the German Federal Ministry of Research, Technology and Space (BMFTR) for funding within the project MELLi (03XP0447). This work was partially supported by BASF SE. The authors acknowledge the use of ChatGPT for language correction and Figure editing.

Supplementary materials

Supplementary material associated with this article can be found, in the online version, at doi:10.1016/j.ensm.2026.105231.

References

[1] J. Janek, W.G. Zeier, Challenges in speeding up solid-state battery development, Nat Energy 8 (2023) 230–240.
[2] J. Janek, W.G. Zeier, A solid future for battery development, Nat Energy 1 (2016) 16141.
[3] Y. Lu, et al., Dry electrode technology, the rising star in solid-state battery industrialization, Matter 5 (2022) 876–898.
[4] D.J. Lee, et al., Robust interface and reduced operation pressure enabled by co-rolling dry-process for stable all-solid-state batteries, Nat Commun 16 (2025) 4200.
[5] Y. Li, et al., Progress in solvent-free dry-film technology for batteries and supercapacitors, Materials Today 55 (2022) 92–109.
[6] D.H.S. Tan, A. Banerjee, Z. Chen, Y.S. Meng, From nanoscale interface characterization to sustainable energy storage using all-solid-state batteries, Nat. Nanotechnol. 15 (2020) 170–180.
[7] J. Li, J. Fleetwood, W.B. Hawley, W. Kays, From Materials to Cell: State-of-the-Art and Prospective Technologies for Lithium-Ion Battery Electrode Processing, Chem. Rev. 122 (2022) 903–956.
[8] J. Zhang, et al., Challenges and Strategies of Low-Pressure All-Solid-State Batteries, Advanced Materials 37 (2025) 2413499.
[9] K.B. Hatzell, Y. Zheng, Prospects on large-scale manufacturing of solid state batteries, MRS Energy & Sustainability 8 (2021) 33–39.
[10] P. Henkel, et al., Beyond Conventional Coatings: Melt-Infiltration of Antiperovskites for High-Voltage All-Solid-State Batteries, ChemElectroChem 12 (2025) e202500286.
[11] J. Oh, et al., Critical impact of volume changes in sulfide-based all-solid-state batteries operating under practical conditions, Energy Storage Materials 71 (2024) 103606.
[12] S. Puls, et al., Benchmarking the reproducibility of all-solid-state battery cell performance, Nat Energy 9 (2024) 1310–1320.
[13] J. Adjah, et al., Effects of external pressure on all-solid-state batteries: comprehensive review and analysis, Energy Storage Materials 81 (2025) 104461.
[14] X. Liu, et al., Electrochemo-Mechanical Effects on Structural Integrity of Ni-Rich Cathodes with Different Microstructures in All Solid-State Batteries, Advanced Energy Materials 11 (2021) 2003583.
[15] G. Li, S. Wang, J. Fu, Y. Liu, Z. Chen, Manufacturing High-Energy-Density Sulfidic Solid-State Batteries, Batteries 9 (2023) 347.
[16] F. Strauss, et al., Impact of Cathode Material Particle Size on the Capacity of Bulk-Type All-Solid-State Batteries, ACS Energy Lett. 3 (2018) 992–996.
[17] N.-Y. Park, et al., High-energy, long-life Ni-rich cathode materials with columnar structures for all-solid-state batteries, Nat Energy 10 (2025) 479–489.
[18] J. Lee, T. Lee, K. Char, K.J. Kim, J.W. Choi, Issues and Advances in Scaling up Sulfide-Based All-Solid-State Batteries, Acc. Chem. Res. 54 (2021) 3390–3402.
[19] C. Singer, S. Schmalzbauer, R. Daub, Influence of the slurry composition on thin-film components for the wet coating process of sulfide-based all-solid-state batteries, Journal of Energy Storage 68 (2023) 107703.
[20] M. Balaish, et al., Emerging processing guidelines for solid electrolytes in the era of oxide-based solid-state batteries, Chem. Soc. Rev. 54 (2025) 8925–9007.
[21] L. Xu, et al., Toward the Scale-Up of Solid-State Lithium Metal Batteries: The Gaps between Lab-Level Cells and Practical Large-Format Batteries, Advanced Energy Materials 11 (2021) 2002360.
[22] T. Ates, M. Keller, J. Kulisch, T. Adermann, S. Passerini, Development of an all-solid-state lithium battery by slurry-coating procedures using a sulfidic electrolyte, Energy Storage Materials 17 (2019) 204–210.
[23] J. Schnell, et al., Prospects of production technologies and manufacturing costs of oxide-based all-solid-state lithium batteries, Energy Environ. Sci. 12 (2019) 1818–1833.
[24] Y. Li, et al., Integrated electro- and chemical characterization of sulfide-based solid-state electrolytes, Mater. Adv. 5 (2024) 9138–9159.
[25] T.A. Yersak, Y. Zhang, F. Hao, M. Cai, Moisture Stability of Sulfide Solid-State Electrolytes, Front. Energy Res. 10 (2022) 882508.
[26] J. Ruhl, L.M. Riegger, M. Ghidiu, W.G. Zeier, Impact of Solvent Treatment of the Superionic Argyrodite Li_6 PS_5 Cl on Solid-State Battery Performance, Adv Energy and Sustain Res 2 (2021) 2000077.
[27] Y.-T. Chen, et al., Investigating dry room compatibility of sulfide solid-state electrolytes for scalable manufacturing, J. Mater. Chem. A 10 (2022) 7155–7164.
[28] J. Mun, T. Song, M. Park, J.H. Kim, Paving the Way for Next-Generation All-Solid-State Batteries: Dry Electrode Technology, Advanced Materials 37 (2025) 2506123.
[29] C. Zihrul, M. Lippke, A. Kwade, Model Development for Binder Migration within Lithium-Ion Battery Electrodes during the Drying Process, Batteries 9 (2023) 455.
[30] M. Stein, A. Mistry, P.P. Mukherjee, Mechanistic Understanding of the Role of Evaporation in Electrode Processing, J. Electrochem. Soc. 164 (2017) A1616–A1627.
[31] J. Kumberg, et al., Drying of Lithium-Ion Battery Anodes for Use in High-Energy Cells: Influence of Electrode Thickness on Drying Time, Adhesion, and Crack Formation, Energy Tech 7 (2019) 1900722.
[32] H. Oh, et al., Development of a feasible and scalable manufacturing method for PTFE-based solvent-free lithium-ion battery electrodes, Chemical Engineering Journal 491 (2024) 151957.
[33] G.A.B. Matthews, S. Wheeler, J. Ramírez-González, P.S. Grant, Solvent-free NMC electrodes for Li-ion batteries: unravelling the microstructure and formation of the PTFE nano-fibril network, Front. Energy Res. 11 (2024) 1336344.
[34] D. Lee, A. Manthiram, Stable Cycling with Intimate Contacts Enabled by Crystallinity-Controlled PTFE-Based Solvent-Free Cathodes in All-Solid-State Batteries, Small Methods 7 (2023) 2201680.
[35] B. Emley, et al., Impact of fabrication methods on binder distribution and charge transport in composite cathodes of all-solid-state batteries, Mater. Futures 2 (2023) 045102.

[36] J. Hong, et al., Optimization of PTFE fibrillation in dry electrode process for scalable all-solid-state battery manufacturing, Journal of Power Sources 655 (2025) 237925.
[37] K. Zhang, et al., Dry Electrode Processing Technology and Binders, Materials 17 (2024) 2349.
[38] Y. Chen, S. Kong, Advances and challenges in dry electrode process for solid-state batteries, J Solid State Electrochem 30 (2026) 1141–1455.
[39] Y.-J. Lee, S.-Y. Kim, W.-J. Song, J. Cha, D.-W. Kim, Enhancing the cycling performance of sulfide-based all-solid-state lithium batteries via molecular weight-dependent fibrillation of PTFE binders, Materials Today Energy 51 (2025) 101914.
[40] D.J. Lee, et al., Physio-Electrochemically Durable Dry-Processed Solid-State Electrolyte Films for All-Solid-State Batteries, Adv Funct Materials 33 (2023) 2301341.
[41] J. Li, et al., Long cycle life all-solid-state batteries enabled by solvent-free approach for sulfide solid electrolyte and cathode films, Chemical Engineering Journal 455 (2023) 140605.
[42] M. Rosner, et al., Analysis of the Electrochemical Stability of Sulfide Solid Electrolyte Dry Films for Improved Dry-Processed Solid-State Batteries, Adv Funct Materials 36 (2025) e18517.
[43] J. Kang, et al., Toward PFAS-free dry electrode processing: Sustainable binder strategies for high-loading electrodes in lithium batteries, Energy Storage Materials 82 (2025) 104662.
[44] S.A. Han, J.H. Suh, M.-S. Park, J.H. Kim, High-Loading Dry-Electrode for all Solid-State Batteries: Nanoarchitectonic Strategies and Emerging Applications, Electrochem. Energy Rev. 8 (2025) 5.
[45] F. Hippauf, et al., Overcoming binder limitations of sheet-type solid-state cathodes using a solvent-free dry-film approach, Energy Storage Materials 21 (2019) 390–398.
[46] P. Minnmann, L. Quillman, S. Burkhardt, F.H. Richter, J. Janek, Editors' Choice—Quantifying the Impact of Charge Transport Bottlenecks in Composite Cathodes of All-Solid-State Batteries, J. Electrochem. Soc. 168 (2021) 040537.
[47] F. Strauss, et al., Influence of electronically conductive additives on the cycling performance of argyrodite-based all-solid-state batteries, RSC Adv. 10 (2020) 1114–1119.
[48] S.-K. Jung, et al., Understanding the effects of chemical reactions at the cathode–electrolyte interface in sulfide based all-solid-state batteries, J. Mater. Chem. A 7 (2019) 22967–22976.
[49] F. Walther, et al., Influence of Carbon Additives on the Decomposition Pathways in Cathodes of Lithium Thiophosphate-Based All-Solid-State Batteries, Chem. Mater. 32 (2020) 6123–6136.
[50] G. Li, The influence of polytetrafluorethylene reduction on the capacity loss of the carbon anode for lithium ion batteries, Solid State Ionics 90 (1996) 221–225.
[51] Q. Wu, J.P. Zheng, M. Hendrickson, E.J. Plichta, Dry Process for Fabricating Low Cost and High Performance Electrode for Energy Storage Devices, MRS Advances 4 (2019) 857–863.
[52] Z. Wei, et al., Removing electrochemical constraints on polytetrafluoroethylene as dry-process binder for high-loading graphite anodes, Joule 8 (2024) 1350–1363.
[53] W. Zhang, et al., Electro)chemical expansion during cycling: monitoring the pressure changes in operating solid-state lithium batteries, J. Mater. Chem. A 5 (2017) 9929–9936.
[54] S. Payandeh, F. Strauss, A. Mazilkin, A. Kondrakov, T. Brezesinski, Tailoring the $LiNbO_3$ coating of Ni-rich cathode materials for stable and high-performance all-solid-state batteries, Nano Research Energy 1 (2022) e9120016.
[55] J.H. Teo, et al., The interplay between (electro)chemical and (chemo)mechanical effects in the cycling performance of thiophosphate-based solid-state batteries, Mater. Futures 1 (2022) 015102.
[56] J. Yang, et al., Glass-Ceramic Lithium Thiophosphate Electrolytes with Enhanced Conductivity and (Chemo)mechanical Properties for All-Solid-State Batteries, Chem. Mater. 37 (2025) 4016–4026.
[57] F. Walther, et al., The Working Principle of a $Li_2CO_3/LiNbO_3$ Coating on NCM for Thiophosphate-Based All-Solid-State Batteries, Chem. Mater. 33 (2021) 2110–2125.
[58] F. Walther, et al., Visualization of the Interfacial Decomposition of Composite Cathodes in Argyrodite-Based All-Solid-State Batteries Using Time-of-Flight Secondary-Ion Mass Spectrometry, Chem. Mater. 31 (2019) 3745–3755.
[59] T. Wagner, M. Rohnke, J. Janek, Long-term degradation study of Polytetrafluoroethylene in a low temperature oxygen plasma, Polymer Degradation and Stability 229 (2024) 110989.
[60] C. Rosenbach, et al., Visualizing the Chemical Incompatibility of Halide and Sulfide-Based Electrolytes in Solid-State Batteries, Advanced Energy Materials 13 (2023) 2203673.
[61] T. Bartsch, et al., Gas Evolution in All-Solid-State Battery Cells, ACS Energy Lett. 3 (2018) 2539–2543.
[62] R. Jung, M. Metzger, F. Maglia, C. Stinner, H.A. Gasteiger, Oxygen Release and Its Effect on the Cycling Stability of $LiNi_xMn_yCo_zO_2$ (NMC) Cathode Materials for Li-Ion Batteries, J. Electrochem. Soc. 164 (2017) A1361–A1377.
[63] T. Hatsukade, A. Schiele, P. Hartmann, T. Brezesinski, J. Janek, Origin of Carbon Dioxide Evolved during Cycling of Nickel-Rich Layered NCM Cathodes, ACS Appl. Mater. Interfaces 10 (2018) 38892–38899.
[64] F. Strauss, et al., Gas Evolution in Lithium-Ion Batteries: Solid versus Liquid Electrolyte, ACS Appl. Mater. Interfaces 12 (2020) 20462–20468.
[65] R. Jung, P. Strobl, F. Maglia, C. Stinner, H.A. Gasteiger, Temperature Dependence of Oxygen Release from $LiNi_{0.6}Mn_{0.2}Co_{0.2}O_2$ (NMC622) Cathode Materials for Li-Ion Batteries, J. Electrochem. Soc. 165 (2018) A2869–A2879.
[66] J. Cha, S. Kim, U.T. Nakate, D.-W. Kim, Highly conductive composite cathode prepared by dry process using Nafion-Li ionomer for sulfide-based all-solid-state lithium batteries, Journal of Power Sources 613 (2024) 234914.
[67] K. Lee, Y. Jo, J. Seok Nam, H. Yu, Y.-J. Kim, Dry-film technology employing cryo-pulverized polytetrafluoroethylene binder for all-solid-state batteries, Chemical Engineering Journal 487 (2024) 150221.
[68] S.-B. Hong, et al., All-Solid-State Lithium Batteries: Li^+-Conducting Ionomer Binder for Dry-Processed Composite Cathodes, ACS Energy Lett 7 (2022) 1092–1100.
[69] D. Lee, et al., Shear force effect of the dry process on cathode contact coverage in all-solid-state batteries, Nat Commun 15 (2024) 4763.
[70] Z. Zhang, L. Wu, D. Zhou, W. Weng, X. Yao, Flexible Sulfide Electrolyte Thin Membrane with Ultrahigh Ionic Conductivity for All-Solid-State Lithium Batteries, Nano Lett 21 (2021) 5233–5239.
[71] Y. Ma, et al., Interface and Electrode Microstructure Engineering for Optimizing Performance of the $LiNiO_2$ Cathode in All-Solid-State Batteries, Chem. Mater. 36 (2024) 2588–2598.
[72] Y. Ma, et al., Single- to Few-Layer Nanoparticle Cathode Coating for Thiophosphate-Based All-Solid-State Batteries, ACS Nano 16 (2022) 18682–18694.